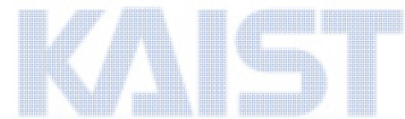


박사학위논문

Ph. D. Dissertation

쉘 구조물 해석을 위한
삼각형 유한요소의 개발

Development of triangular finite elements for
analysis of shell structures



한국과학기술원



SINCE 1971

이윤규(李淪圭 Lee, Youngyu)

기계항공시스템학부 해양시스템공학전공

School of Mechanical, Aerospace and Systems Engineering,

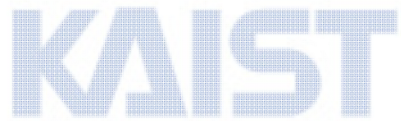
Division of Ocean Systems Engineering

KAIST

2015

쉘 구조물 해석을 위한
삼각형 유한요소의 개발

Development of triangular finite elements for
analysis of shell structures



한국과학기술원



SINCE 1971

Development of triangular shell finite elements for analysis of shell structures

Advisor: Professor Phill-Seung Lee

by

Youngyu Lee

School of Mechanical, Aerospace and Systems Engineering,

Division of Ocean Systems Engineering

KAIST

A thesis submitted to the faculty of KAIST in partial fulfillment of requirements for the degree of Doctor of Philosophy in the School of Mechanical, Aerospace and Systems Engineering, Division of Ocean Systems Engineering. The study was conducted in accordance with Code of Research Ethics¹



November 14, 2014

Approved by

Professor Phill-Seung Lee

¹Declaration of Ethical Conduct in Research: I, as a graduate student of KAIST, hereby declare that I have not committed any acts that may damage the credibility of my research. These include, but are not limited to: falsification, thesis written by someone else, distortion of research findings or plagiarism. I affirm that my thesis contains honest conclusions based on my own careful research under the guidance of my thesis advisor.

Development of triangular shell finite elements for analysis of shell structures

Youngyu Lee

The present dissertation has been approved by the dissertation committee
as a Ph. D. dissertation at KAIST



Committee member K. C. Park

Committee member Hyun Chung

Committee member Yeunwoo Cho

Committee member Do-Nyun Kim

DOSE
20115216

이윤구 Lee, Youngyu. Development of triangularfinite elements for analysis of shell structures *쉘구조물해석을위한삼각형유한요소의개발*. School of Mechanical, Aerospace and Systems Engineering, Division of Ocean Systems Engineering. 2015. 149p. Advisor Prof. Lee, Phill-Seung. Text in English

ABSTRACT

Shells structures have been frequently used in various engineering fields. The finite element method has been dominantly used to analyze shell structures over the past several decades. However, although a great effort has been expended to develop an effective 3-node triangular shell finite element, no element is currently available that has been shown to be reliable and effective in the analysis of general shell structures.

The purpose of this thesis is to develop an effective 3-node triangular shell finite element in analysis of general shell structures. Such element should show isotropic behavior and pass the consistency, ellipticity and inf-sup conditions and hence be optimal in convergence regardless of the shell geometry, thickness of the shell, boundary conditions and applied loading.

An improved 3-node MITC3 triangular shell finite element is developed. The Hellinger-Reissner (HR) variational principle is modified in the framework of the MITC method, and a special approximated transverse shear strain field is proposed. The MITC3-HR shell finite element improved using the Hellinger-Reissner functional passes all of the basic tests (the zero energy mode test, the patch test, and the isotropic element test). Convergence studies considering plate and shell benchmark problems demonstrate the improved predictive capability of the MITC3-HR shell finite element.

An effective new 3-node MITC3+ triangular shell finite element is developed for general use. A cubic bubble function for the interpolation of the rotations is used to enrich the bending displacements. To reduce shear locking in the shell element, a new assumed transverse shear strain field is designed with a new tying scheme to reduce locking while satisfying the consistency and ellipticity conditions. The MITC3+ shell element passes all basic tests, that is, the isotropy, zero energy mode and patch tests, and shows an excellent convergence behavior in the solution of plate and shell benchmark problems even when severely distorted meshes are used.

The static and dynamic modal behavior of the MITC3+ triangular shell element is investigated. For comparison, the pure displacement-based (DISP3), MITC3 and MITC4 shell elements are also studied. First, static mode solutions are performed for a single right-angled shell element and an assemblage of two right-angled shell elements. Detailed strain fields are established in the bending modes. This study provides insight into how shear locking occurs on the mode level. We then analytically show how the MITC3+ shell element properly represents the pure bending conditions in a two-sided clamped plate problem. Considering free vibration shell problems, we finally present the excellent performance of the MITC3+ shell element in dynamic mode solutions.

Keywords: Shell Structures; Shell finite elements; 3-Node element; MITC method; Convergence

Table of Contents

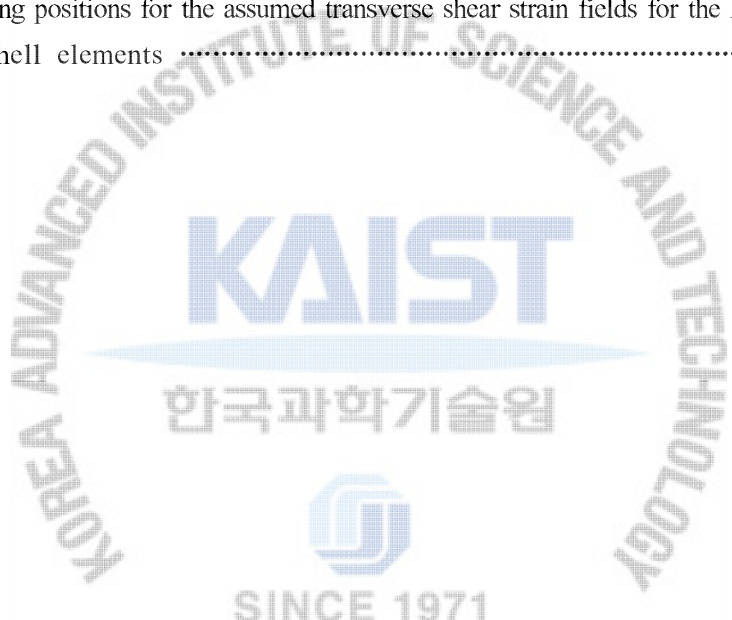
Abstract	i
Table of Contents	ii
List of Tables	iv
List of Figures	vi
Chapter 1. Introduction	1
Chapter 2. Finite element analysis of shells	4
2.1 The asymptotic behavior of shell structures	4
2.1.1 Fundamental asymptotic theory	4
2.1.2 Layers and characteristic length	7
2.1.3 Asymptotic analysis	7
2.2 Continuum mechanics based shell element	8
2.3 Locking phenomenon and locking treatment	9
2.3.1 Reduced Integration	10
2.3.2 Enhanced Assumed Strain method	10
2.3.3 Hellinger-Reissner principle	11
2.3.4 Mixed Interpolation of Tensorial Components method	11
2.4 The ideal shell finite element	12
Chapter 3. Improving the MITC3shell finite element	15
3.1 Formulation of the 3-node displacement-based shell finite element	15
3.2 Formulation of the MITC3 shell finite element.....	17
3.3 The Hellinger-Reissner principle for 3-node shell finite elements.....	22
3.4 Formulation of the MITC3-HR shell finite element.....	24
3.5 Basic numerical tests.....	26
3.5.1 Strain energy mode tests	27
3.5.2 Isotropy test.....	32
3.5.3 Patch test.....	33
3.6 Convergence studies.....	34
3.5.1 Fully clamped square plate problem.....	35
3.5.2 Simply supported sixty-degreeskew plate problem.....	38
3.5.3 Cylindrical shell problems.....	39
3.5.4 Hyperboloid shell problems.....	43
3.7 Closure	47
Chapter 4. MITC3+ shell finite element	48
4.1 Geometry and displacement interpolation.....	48

4.2 Assumed transverse shear strain field.....	49
4.3 Basic numerical tests.....	54
4.4 Convergence studies.....	57
4.4.1 Fully clamped square plate problem.....	57
4.4.2 Simply supported sixty-degreeskew plate problem.....	57
4.4.3 Cylindrical shell problems.....	61
4.4.4 Hyperboloid shell problems.....	66
4.5 Closure.....	71
Chapter 5. Modal behavior of MITC3+ shell finiteelement	72
5.1 Formulations of 3-node triangular shell elements.....	72
5.1.1 The DISP3 shell element.....	73
5.1.2 The MITC3 shell element.....	73
5.1.3 The MITC3+ shell element.....	74
5.2 Static mode analysis.....	75
5.2.1 Single right-angled triangular element.....	76
5.2.2 Assemblage of two right-angled triangular elements.....	83
5.3 Two-sided clamped plate problem.....	89
5.3.1 Transverse shear strain fields.....	90
5.3.2 Strain energy.....	92
5.4 Dynamic mode analysis.....	93
5.4.1 Free square plate problem.....	94
5.4.2 Free hyperboloid shell problem.....	99
5.5Closure.....	108
Chapter 6. Performance of 3-node shell elements for classical benchmark problems.....	109
6.1 Fully clamped square plate problem.....	110
6.2 Morley's thirty-degree skew plate problem.....	113
6.3 Scordelis-Lo roof problem.....	113
6.4 Pinched cylindrical shell problem.....	116
6.5 Hemispherical shell problem.....	117
6.6 Effects of mesh distortion.....	120
6.6.1 Distorted mesh A.....	120
6.6.2 Distorted mesh B.....	120
6.7 Closure.....	125
Chapter 7. Conclusions.....	126
Appendix A.Mode decomposition of the 3-node plate element.....	128
Appendix B. Assumed transverse shear strain fields for a 3-node shell element.....	134
Appendix C.Transverse shear strain fields of the MITC3+ element in flat geometry	141
References.....	142
Summary.....	149

List of Tables

Table 2.1 The asymptotic categories of shell behaviors	6
Table 2.2 Asymptotic categories for shell problems	8
Table 3.1 Results of basic numerical tests.....	27
Table 3.2 The eigenvalues of the strain energy modes of the MITC3-HR shell finite element for the plate bending problem shown in Fig. 3.8(a) when $t/L = 1/1,000$	29
Table 3.3 The eigenvalues of the strain energy modes of the MITC3-HR shell finite element for the plate bending problem shown in Fig. 3.8(a) when $t/L = 1/10,000$	29
Table 3.4 Input values for the geometry shown in Fig. 3.10 for the isotropic test.....	32
Table 4.1 Tying positions for the new assumed transverse shear strain field for the MITC3i and MITC3+ shell elements.....	53
Table 4.2 Results of basic numerical tests.....	54
Table 4.3 Eigenvalues of the stiffness matrix of the single MITC3i shell element for the element geometry shown in Fig. 4.2(a) when $t/L = 1/10,000$	56
Table 4.4 Eigenvalues of the stiffness matrix of the single MITC3+ shell element for the element geometry shown in Fig. 4.2(a) when $t/L = 1/10,000$	56
Table 5.1 Eigenvalues of the stiffness matrices of the single triangular shell element for the element geometry shown in Fig. 5.1.....	78
Table 5.2 Strain fields of the single right-angled DISP3 and MITC3 shell elements in the bending modes B1, B2 and B3.....	81
Table 5.3 Strain fields of the single right-angled MITC3+ shell element in the bending modes B1+ and B2+, and in-plane twisting mode T.....	82
Table 5.4 Eigenvalues of an assemblage of two right-angled triangular shell elements shown in Fig. 5.4 when $a/L = 1/10,000$	86
Table 5.5 Eigenvalues of the stiffness matrix for the assemblage of two MITC3+ shell elements shown in Fig. 5.4(b) according to the tying distance d in the plate bending problem when $a/L = 1/10,000$	87
Table 5.6 Strain fields of the MITC4, MITC3 and MITC3+ shell element in the bending mode BL1.....	88
Table 5.7 Strain energies for the two-sided clamped plate problem shown in Fig. 5.7	92
Table 5.8 Strain energies for the two-sided clamped plate problem shown in Fig. 5.7 using the Mesh A with the MITC3+ shell elements according to the tying distance d	93
Table 5.9 Frequencies of the modes 7-11 for the free plate problem shown in Fig. 5.9 with $N \times N$ meshes when $a/L = 1/1,000$	96

Table 5.10 Frequencies of the modes 7-11 for the free plate problem shown in Fig. 5.12 with $N \times N$ distorted meshes when $a/L = 1/1,000$	100
Table 5.11 Frequencies of the modes 7-12 for the free hyperboloid shell problem with the $4N \times 2N$ uniform meshes shown in Fig. 5.14(a) when $a/L = 1/1,000$	103
Table 5.12 Frequencies of the modes 7-12 for the free hyperboloid shell problem with the $4N \times 2N$ distorted meshes shown in Fig. 5.14(b) when $a/L = 1/1,000$	106
Table 6.1 Strain energy for the fully clamped plate problem under uniform pressure with the distorted mesh shown in Fig. 6.13.....	122
Table 6.2 Strain energy for the quarter of an infinitely long cylinder with the distorted mesh shown in Fig. 6.13.....	123
Table A.1 Tying positions for the assumed transverse shear strain field in the antisymmetrical bending and shearing modes	131
Table B.1 Tying positions for the assumed transverse shear strain fields for the MITC3i-a and MITC3i-b shell elements	136



List of Figures

Fig. 2.1 Curved surface depending on the Gaussian curvature	8
Fig. 2.2 Tying positions for the assumed transverse shear strain field of the MITC4 shell element.....	13
Fig. 3.1A standard 3-node triangular continuum mechanics based shell finite element.....	16
Fig. 3.2 Transverse shear strain relation.....	18
Fig. 3.3Tying positions for the assumed transverse shear strain field of the MITC3 shell element.....	18
Fig. 3.4 The nodal displacement pattern of the physical strain energy modes at the top view.....	19
Fig. 3.5 The constant transverse shear strain condition and tying positions for the symmetrical bending modes, $\tilde{e}_{qt} = (\tilde{e}_{st} - \tilde{e}_{rt})/\sqrt{2}$	21
Fig. 3.6 Therotated covariant base vectors for the MITC3-HR shell finite element.....	25
Fig. 3.7Strain energy mode test ($L = 1.0$, $E = 1.7472 \times 10^7$ and $\nu = 0.3$).....	28
Fig. 3.8 Shapes of the normalized 10th strain energy mode.....	30
Fig. 3.9 Ratio of the strain energy of the MITC3-HR shell finite element to the strain energy of the MITC3 shell finite element depending on the rotation angle (θ) of the contravariant base vectors in the in-plane twisting mode.....	30
Fig. 3.10 A single 3-node triangular shell finite element for the isotropic test.....	32
Fig. 3.11 Triangular mesh used for the patch tests.....	33
Fig. 3.12 Fully clamped square plate problem under uniform pressure ($L=1.0$, $E = 1.7472 \times 10^7$, $q=1.0$ and $\nu=0.3$) with 2 different 4×4 mesh patterns in (a) and (b).....	35
Fig. 3.13 Convergence curves for the fully clamped square plate problem.....	36
Fig. 3.14Distorted mesh patterns	37
Fig. 3.15Convergence curves for the fully clamped square plate problemwith the distorted meshes shown in Fig. 3.14.....	37
Fig. 3.16 Simply supported sixty-degree skew plate problem ($L=1.0$, $E = 1.7472 \times 10^7$ and $\nu = 0.3$).....	38
Fig. 3.17 Convergence curves for the simply supported sixty-degree skew plate problem.....	39
Fig. 3.18Cylindrical shell problem (4×4 mesh, $L = R = 1.0$, $E = 2.0 \times 10^5$, $\nu = 1/3$ and $p_0 = 1.0$).....	40
Fig. 3.19 Convergence curves for the clamped cylindrical shell problem.....	41
Fig. 3.20 Convergence curves for the free cylindrical shell problem.....	41
Fig. 3.21 Convergence curves for the clamped cylindrical shell problemwith the distorted meshes shown in Fig. 3.14.....	42

Fig. 3.22 Convergence curves for the free cylindrical shell problemwith the distorted meshes shown in Fig. 3.14.....	42
Fig. 3.23Hyperboloid shell problem ($E=2.0\times10^{11}$, $\nu=1/3$ and $p_0=1.0$).....	44
Fig. 3.24 Convergence curves for the clamped hyperboloid shell problem.....	45
Fig. 3.25 Convergence curves for the freehyperboloid shell problem.....	45
Fig. 3.26 Convergence curves for the clamped hyperboloid shell problemwith the distorted meshes shown in Fig. 3.14.....	46
Fig. 3.27 Convergence curves for the freehyperboloid shell problemwith the distorted meshes shown in Fig. 3.14.....	46
Fig. 4.1Geometry of the MITC3+ shell elementwithan additional bubble node	49
Fig. 4.2In-plane twisting mode of a single shell finite element.....	50
Fig. 4.3 Transverse shear strains e_{1t} , e_{2t} and e_{3t} , and the tying positions (A)-(F)for the new assumed transverse shear strain field.....	51
Fig. 4.4 Strain energy stored in the MITC3i and MITC3+ shell elements depending on the distance d in the in-plane twisting mode.....	55
Fig. 4.5 Convergence curves for the fully clamped square plate problem.....	58
Fig. 4.6 Convergence curves for the fully clamped square plate problemwith the distorted meshes shown in Fig. 3.14	59
Fig. 4.7 Convergence curves for the simply supported sixty-degree skew plate problem.....	60
Fig. 4.8 Convergence curves for the clamped cylindrical shell problem.....	62
Fig. 4.9 Convergence curves for the free cylindrical shell problem.....	63
Fig. 4.10 Convergence curves for the clamped cylindrical shell problemwith the distorted meshes shown in Fig. 3.14	64
Fig. 4.11 Convergence curves for the free cylindrical shell problemwith the distorted meshes shown in Fig. 3.14	65
Fig. 4.12 Convergence curves for the clamped hyperboloid shell problem.....	67
Fig. 4.13 Convergence curves for the freehyperboloid shell problem.....	68
Fig. 4.14 Convergence curves for the clamped hyperboloid shell problemwith the distorted meshes shown in Fig. 3.14	69
Fig. 4.15 Convergence curves for the freehyperboloid shell problemwith the distorted meshes shown in Fig. 3.14	70
Fig. 5.1 A single right-angled triangular shell element for plate bending problem ($L=1.0$, $a/L=1/10,000$, $E=1.7472\times10^7$ and $\nu=0.3$).....	76
Fig. 5.2 Shapes of the bending modes for the single right-angled MITC3 shell element shown in Fig. 5.1(a).....	79
Fig. 5.3 Mode shapes of the single right-angled MITC3+ shell element shown in Fig. 5.1(b)	80
Fig. 5.4 An assemblage of two right-angled triangular elements ($L=1.0$, $E=1.7472\times10^7$ and $\nu=0.3$).....	83

Fig. 5.5 Shapes of the bending mode BL1 shown in Fig. 5.4.....	85
Fig. 5.6 In-plane twisting of two 3-node triangular shell elements.....	88
Fig. 5.7 Two-sided clamped plate problem ($L=1.0$, $m_\alpha = m_\beta = 2/L$, $E = 1.7472 \times 10^7$ and $\nu = 0.0$) and meshes used for the MITC3+shell elements (Meshes A and B) and the MITC4 shell elements (Mesh C).....	89
Fig. 5.8 Element node numbers for the two-sided clamped plate problem using the MITC3+ shell elements with Mesh A shown in Fig. 5.7.....	90
Fig. 5.9 Free square plate problem for dynamic mode analyses with 2 different 5×5 mesh patterns ($L=1.0$, $E = 2.07 \times 10^{11}$, $\nu = 0.3$ and $\rho = 7.8 \times 10^3$).....	95
Fig. 5.10 Shapes of the modes 7-11 for the free plate problem shown in Fig. 5.9 with 5×5 element meshes when $a/L = 0.001$	97
Fig. 5.11 Convergence curves of the 10th and 11th frequencies for the free plate problem.....	98
Fig. 5.12 Distorted mesh pattern for $N = 5$	99
Fig. 5.13 Convergence curves of the 10th and 11th frequencies for the free plate problem with the distorted meshes shown in Fig. 5.12	101
Fig. 5.14 Free hyperboloid shell problem ($L=1.0$, $E = 2.0 \times 10^{11}$, $\nu = 1/3$ and $\rho = 7.8 \times 10^3$)	102
Fig. 5.15 Shapes of the modes 7-12 for the free hyperboloid shell problem shown in Fig. 14(a) with 20×10 element meshes when $a/L = 0.001$	104
Fig. 5.16 Convergence curves of the 7th and 8th frequencies for the free hyperboloid shell problem with the uniform meshes shown in Fig. 5.14(a)	105
Fig. 5.17 Convergence curves of the 7th and 8th frequencies for the free hyperboloid shell problem with the distorted meshes shown in Fig. 5.14(b)	107
Fig. 6.1 Fully clamped square plate problem ($L=1.0$, $E = 1.7472 \times 10^7$ and $\nu = 0.3$).....	110
Fig. 6.2 Convergence curves of the normalized displacements (w_C) for the fully clamped square plate problem under the concentrated load	111
Fig. 6.3 Convergence curves of the normalized displacements (w_C) for the fully clamped square plate problem under the uniform pressure	112
Fig. 6.4 Morley's thirty-degree skew plate problem ($L = 100$, $E = 1.0 \times 10^7$ and $\nu = 0.3$).....	113
Fig. 6.5 Convergence curves of the normalized central displacements (w_{center}) for the Morley's thirty-degree skew plate problem	114
Fig. 6.6 Scordelis-Lo roof problem ($R = 25$, $L = 50$, $t = 0.25$, $E = 4.32 \times 10^8$ and $\nu = 0.0$)	115
Fig. 6.7 Convergence curves of the normalized displacements (w_B) for the Scordelis-Lo roof problem	115
Fig. 6.8 Pinched cylindrical shell problem with the two end conditions: rigid diagrams ($R = 1.0$,	

$L=1.0$, $t=0.01$, $E=3.0 \times 10^7$ and $\nu=0.3$) and free ends ($R=4.953$, $L=5.175$, $E=10.5 \times 10^6$ and $\nu=0.3125$).....	116
Fig. 6.9 Convergence curves of the normalized displacements (w_C) for the pinched cylindrical shell problem with the rigid diagrams.....	117
Fig. 6.10 Convergence curves of the normalized displacements(w_C) for the pinched cylindrical shell problem with the free ends	118
Fig. 6.11 Hemispherical shell problem ($R=10$, $t=0.04$, $p=1.0$, $E=6.825 \times 10^7$ and $\nu=0.3$).....	119
Fig. 6.12 Convergence curves of the normalized displacements(u_A) for the hemispherical shell problem.....	119
Fig. 6.13 Fully clamped square plate problem under uniform pressure ($L=10$, $E=1000$, $q=10$ and $\nu=0.3$).....	121
Fig. 6.14 Quarter of an infinitely long cylinder under constant bending ($R=10$, $L=10$, $E=1000$ and $\nu=0.3$).....	122
Fig. 6.15 Distorted mesh patterns for the cylindrical shell problem.....	123
Fig. 6.16 Convergence curves of the normalized displacements(w_C) for the pinched cylindrical shell problem with the free ends using the distorted meshes shown in Fig 6.15.....	124
Fig. 6.17 Convergence curves of the normalized displacements(u_A) for the hemispherical shell problem using the distorted meshes shown in Fig 6.15.....	125
Fig. A.1 In-plane twisting mode when a single 3-node plate element is twisted at the barycenter.....	129
Fig. A.2 The nodal displacement pattern of the physical antisymmetrical bending and shearing strain energy modes (type A) at the top view	130
Fig. A.3 Tying positions for assumed transverse shear strain fields in the antisymmetrical bending and shearing modes.....	130
Fig. A.4 Convergence curves for the fully clamped square plate problem.....	132
Fig. A.5 The nodal displacement pattern of the physical antisymmetrical bending and shearing strain energy modes (type B) at the top view	133
Fig. B.1 Transverse shear strains.....	136
Fig. B.2 Tying positions for the assumed transverse shear strain field	137
Fig. B.3 Convergence curves for the fully clamped square plate problem.....	138
Fig. B.4 Convergence curves for the clamped cylindrical shell problem.....	138
Fig. B.5 Convergence curves for the free cylindrical shell problem.....	139
Fig. B.6 Convergence curves for the clamped hyperboloid shell problem.....	139
Fig. B.7 Convergence curves for the free hyperboloid shell problem.....	140

Chapter 1. Introduction

Shells structures have been frequently used in various engineering fields. The finite element method has been mainly used to analyze shell structures over the past several decades. For an analysis of shells, it is crucial to use reliable and effective shell finite elements. However, it is still challenging to develop such shell finite elements due to the highly sensitive and complex behaviors of shells [1, 2]. In particular, it is important to develop an effective 3-node triangular shell element, which is very useful for automatic mesh generations for complex shell structures due to its simple geometry defined by only three corner nodes. In addition, an effective 3-node triangular shell element would be attractive due to the small bandwidth of the governing global stiffness and mass matrices [1-13].

An ideal shell finite element should uniformly converge with the optimal rate regardless of the three asymptotic behaviors of membrane dominated, bending dominated and mixed behaviors depending on the shell geometry, boundary conditions and applied loadings. Of course, the shell element should satisfy the ellipticity and consistency. The main difficulty related to a shell finite element analysis is that the solution accuracy becomes worse as the shell thickness becomes smaller [14-18]. This is called locking, which occurs when the shell element formulation cannot represent pure bending displacement fields suitably [1, 2].

To reduce the locking behavior, the Mixed Interpolation of Tensorial Components (MITC) method was first used to develop a 4-node shell element (MITC4) [19, 20]. Then, for higher-order quadrilateral elements, a 9-node shell element (MITC9) and a 16-node shell element (MITC16) were developed [21, 22]. Later, the method was applied to develop a 3-node triangular shell element (MITC3) as well as higher-order triangular shell elements [10, 23]. However, the performance of the MITC3 triangular shell element is not as good as the MITC4 quadrilateral shell element, despite the fact that the MITC3 triangular shell element performs much better than the displacement-based 3-node triangular shell element (DISP3) [11].

The purpose of this thesis is to develop an effective 3-node triangular shell finite element in analysis of general shell structures. Such element should present isotropic behavior and pass the consistency, ellipticity and inf-sup conditions and hence should be optimal in convergence tests for general shell structures. Also, the formulation can directly be extended for nonlinear analysis of shells.

A 3-node MITC3-HR triangular shell element is developed. We modify the Hellinger-Reissner functional and introduce a special approximated transverse shear strain field based on rotated contravariant bases. The MITC3-HR element passes all basic tests, that is, theisotropy, zero energy mode and patch tests. The well-established convergence studies numerically show that the MITC3 shell finite element is successfully improved [12].

An effective new 3-node MITC3+ triangular shell finite element is developed. The MITC3+ shell element uses a cubic bubble function for the interpolation of the rotations to enrich the bending displacement fields. The corresponding rotation degrees of freedom can be statically condensed out on the element level. A new assumed transverse shear strain field was developed with a new tying scheme to reduce shear locking while satisfying the consistency and ellipticity conditions. The MITC3+ shell element passes all basic tests, that is, theisotropy, zero energy mode and patch tests, and shows an excellent convergence behavior in the solution of plate and shell benchmark problems, even when severely distorted meshes are used [24].

A deeper understanding of the MITC3+ shell element is obtained through detailed static and dynamic mode solutions. The DISP3, MITC3 and MITC4 shell elements are also considered for comparisons. In the static mode solutions of a single right-angled triangular element and an assemblage of two right-angled triangular elements, we investigate the transverse shear strain fields in the bending modes. This study shows how the MITC3+ shell element performs on the mode level. The transverse shear strain fields of the MITC3+ shell element are also studied analytically in a two-sided clamped plate problem, to see whether and how locking occurs. Considering a free vibration shell problems, the excellent performance of the MITC3+ shell element is presented in the dynamic mode solutions [25].

In chapter 1, the introduction is presented.

In chapter 2, the finite element analysis of shells is briefly reviewed. The asymptotic behavior of shell structures, the continuum mechanics based shell element, the locking phenomenon and locking treatment and the ideal shell finite elements are explained.

In chapter 3, the 3-node MITC3-HR triangular shell element based on the Hellinger-Reissner principle is developed. We propose a method that involves the use of the modified Hellinger-Reissner functional to improve the MITC3 shell finite element, after which we explain how to construct the special approximated transverse

shear strain field. Numerical tests are conducted for the MITC3-HR shell element in various shell problems.

In chapter 4, a new 3-node MITC3+ triangular shell finite element was developed. The MITC3+ shell element uses a cubic bubble function for the interpolation of the rotations to enrich the bending displacement fields. A new assumed transverse shear strain field was developed with a new tying scheme to reduce shear locking while satisfying the consistency and ellipticity. Numerical tests are conducted for the MITC3+ shell element in various shell problems.

In chapter 5, a deeper understanding of the MITC3+ shell element is obtained from detailed static and dynamic mode analyses. We investigate eigenvalues and strain fields of the shell elements in static mode analysis and analyze the transverse shearing behavior of the MITC3+ shell element. We then analytically show that the MITC3+ shell element does not lock in the two-sided clamped plate problem. In dynamic mode analysis, the performance of the MITC3+ shell element is presented.

In chapter 6, we perform the convergence tests for the classical benchmark shell problems using the 3-node MITC triangular shell elements in comparison with other 3-node triangular shell elements.

In chapter 7, we present conclusions.

Chapter 2. Finite element analysis of shells

In this chapter, the fundamental theory for the finite element analysis of shells is briefly reviewed. The asymptotic behavior of shell structures, the continuum mechanics based shell element, the locking phenomenon and locking treatment and the ideal shell finite element are explained.

2.1 The asymptotic behavior of shell structures

Shell structures are supported by three basic loading-bearing mechanisms, that is, bending action, membrane action and shearing action. With applied loads, shell structures store the bending strain energy, membrane strain energy and shear strain energy corresponding to these three basic loading-bearing mechanisms, respectively. Because the shear strain energy is negligible when the thickness is small, the strain energy of shells mainly include the bending strain energy and membrane strain energy [2, 14-16, 26].

Depending on shell geometries, boundary conditions, and applied loadings, shell structures present the asymptotic behavior as the thickness is reduced. The behavior of shell structures can be sorted into one of the three asymptotic categories: membrane-dominated, bending-dominated, or mixed shell behavior [16].

2.1.1 Fundamental asymptotic theory

For the linear Naghdi shell model or Koiter shell model, the general variational form follows [2, 16]:

Find $\vec{U}^\lambda \in \vec{\Phi}$ such that

$$\lambda^3 A_b(\vec{U}^\lambda, \vec{V}) + \lambda A_m(\vec{U}^\lambda, \vec{V}) = \vec{F}^\lambda(\vec{V}), \quad \forall \vec{V} \in \vec{\Phi} \quad (2.1)$$

where λ is the shell thickness relative to the overall characteristic length (t/L), A_b is the bilinear form of the scaled bending energy, A_m is the bilinear form of the scaled membrane and shear energies, and \vec{U}^λ is the unknown solution for the displacement field. \vec{V} is the test function, $\vec{\Phi}$ is the Sobolev space in which to

findsolutions, and \vec{F}^λ is the external virtual work connected to \vec{V} . Because the shear strains energyis much lower than the membrane energy when the thickness is thin, λA_m mainly corresponds to the membrane energy in shell structures [16, 26].

As λ goes to zero, the scaled loading in this form is given to establish the asymptotic behavior

$$\vec{F}^\lambda(\vec{V}) = \lambda^\rho G(\vec{V}) \quad (2.2)$$

where ρ is the load-scaling factor. Because the left part of Eq.(2.1) is proportional to λ and λ^3 , ρ is between 1 and 3($1 \leq \rho \leq 3$).

The given space is important when determining the asymptotic behavior

$$\vec{\Psi}_0 = \left\{ \vec{V} \in \vec{\Phi} \mid A_m(\vec{V}, \vec{V}) = 0 \right\} \quad (2.3)$$

Here, $\vec{\Psi}_0$ is the subspace that represents pure bending displacements without the membrane and shear strain energies. When this subspace contains only a zero displacement field ($\vec{\Psi}_0 = \{0\}$), the pure bending is inhibited in a shell structure or the inhibited shell is called. On the other hand, when the subspace contains only a non-zero displacement field ($\vec{\Psi}_0 \neq \{0\}$), the pure bending is non-inhibited in a shell structure or the non-inhibited shell is called [16, 26].

If the pure bending is non-inhibited, the membrane energy term in Eq.(2.1) disappears with $\rho = 3$. The general form of the bending-dominated problem is as follows:

Find $\vec{U}^0 \in \vec{\Phi}_0$ such that

SINCE 1971

$$A_b(\vec{U}^0, \vec{V}) = \vec{G}(\vec{V}), \quad \forall \vec{V} \in \vec{\Phi}_0 \quad (2.4)$$

This problem is shown only when the loading activates the pure bending displacements. If the loading does not result in pure bending displacements, the subspace is as follows:

$$\vec{G}(\vec{V}) = 0, \quad \forall \vec{V} \in \vec{\Phi}_0. \quad (2.5)$$

The shell behavior does not converge to the solution of the bending-dominated shell problem. This asymptotic behavior is like a case in which pure bending is inhibited but very unstable. If only a small change in the loading without satisfying the condition in Eq.(2.5) will lead to the bending-dominated case [2, 16, 26].

If the pure bending is inhibited, the load-scaling factor $\rho = 1$ is used and the shell problem is well-

posed with only the membrane and shear strain energies in the space $\vec{\Phi}_m$. This space is larger than $\vec{\Phi}$ because only the bounded membrane and shear strain energies are considered. The general form of the membrane-dominated problem is as follows:

Find $\vec{U}^m \in \vec{\Phi}_m$ such that

$$A_m(\vec{U}^m, \vec{V}) = \vec{G}(\vec{V}), \quad \forall \vec{V} \in \vec{\Phi}_m \quad (2.6)$$

and this problem is well-posed when the loading \vec{G} is the dual space of $\vec{\Phi}_m$. The condition $\vec{G} \in \vec{\Phi}'_m$ is equivalent to

$$|\vec{G}(\vec{V})| \leq C\sqrt{A_m(\vec{V}, \vec{V})}, \quad \forall \vec{V} \in \vec{\Phi}_m \quad (2.7)$$

where C is constant. The corresponding load is the admissible membrane loading with the condition $\vec{G} \in \vec{\Phi}'_m$. In this applied loading condition, shell structures can be resisted by membrane energy only. If the loading is an non-admissible membrane loading ($\vec{G} \notin \vec{\Phi}'_m$), an ill-posed membrane problem is obtained. Because the asymptotic behavior is not supported by only the membrane energy, the shell behavior is classified as a mixed problem [16, 26].



Table 2.1 The asymptotic categories of shell behaviors [16, 26].

Case	Category	Loading
Non-inhibited shell $\vec{\Phi}_0 \neq \{0\}$	Bending-dominated	Loading activates pure bending displacements $\exists \vec{V} \in \vec{\Phi}_0$ such that $\vec{G}(\vec{V}) \neq 0$
	Membrane-dominated or mixed but unstable	Loading activates pure bending displacements $\vec{G}(\vec{V}) = 0, \quad \forall \vec{V} \in \vec{\Phi}_0$
Inhibited shell $\vec{\Phi}_0 = \{0\}$	Membrane-dominated	Admissible membrane loading $\vec{G} \in \vec{\Phi}'_m$
	Mixed	Non-admissible membrane loading $\vec{G} \notin \vec{\Phi}'_m$

Table 2.1 summarizes the asymptotic categories of the different shell behaviors. The asymptotic behaviors are important when attempting to determine the shell loading capacity. The stiffness of shells is changed with λ^ρ . To demonstrate the shell response accurately, it is necessary to understand shell asymptotic behaviors.

2.1.2 Layers and characteristic length

The stress fields of shells are classified into global smooth parts and various layer parts. The layers arise due to discontinuities in the geometry (curvature or thickness), incompatibilities of the boundary conditions, and irregular loading. In the layers, the stresses, strains and displacements change extremely and the strain energy is concentrated. The characteristic length of the layer of shells is a function of the thickness(t) and the overall length of the shell structure(L)

$$L_c = ct^{1-l} L^l \quad (2.8)$$

Here, c is constant and l is a non-negative real number [16, 26]. In Ref.[16], as the thickness becomes small, the boundary layer of the Scodelis-Lo roof shell problem, the inner layer of the hyperbolic paraboloid shell problem and other type of layers for shells are present.

2.1.3 Asymptotic analysis

Based on theory, a great deal of research has been constructed to determine shell asymptotic behaviors. However, this task is still very difficult. Recently, Lee and Bathe propose the simple method to determine the shell asymptotic behaviors using the finite element analysis [16]. The loading scaling factor ρ is given by

$$\rho \approx \frac{\log E(\lambda + \Delta\lambda) - \log E(\lambda)}{\log(\lambda + \Delta\lambda) - \log \lambda} \quad (2.9)$$

where E is the strain energy for $\lambda (= t/L)$ using the finite element analysis [26]. The more accurate the finite element solution is for a given value of $\lambda (= t/L)$, the more accurate the loading scaling factor is when calculated. A membrane-dominated shell problem arises when $\rho = 1$. Abending-dominated shell problem arises when $\rho = 3$. A mixed shell problem results when $1 < \rho < 3$. The asymptotic categories of shell problems are summarized in Table 2.2 according to the loading scaling factor ρ with the Gaussian curvatures shown in Fig. 2.1 [26].

Table 2.2 Asymptotic categories for shell problems [26].

Asymptotic behavior(ρ)	Shell problems	Gaussian curvature
Membrane-dominated($\rho = 1$)	Fixed cylindrical shell problem	Zero
	Fixed hyperboloid shell problem	Negative
	Clamped hemispherical cap problem	Positive
	Modified Scodelis-Lo roof shell problem	Zero
Bending-dominated($\rho = 3$)	Fully clamped plate problem	Zero
	Free cylindrical shell problem	Zero
	Free hyperboloid shell problem	Negative
	Partly clamped hyperbolic paraboloid shell problem	Negative
Mixed($1 < \rho < 3$)	Scodelis-Lo roof shell problem($\rho = 1.75$)	Zero
Not well-defined	Monster shell problem	Positive

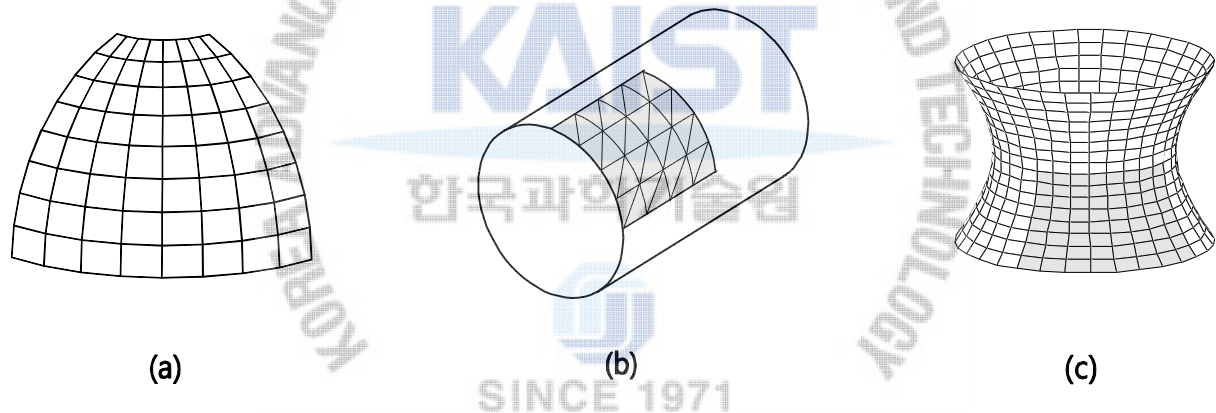


Fig. 2.1 Curved surface depending on the Gaussian curvature. (a) Positive Gaussian curvature. (b) Zero Gaussian curvature. (c) Negative Gaussian curvature.

2.2 The continuum mechanics based shell element

Two basic concepts are used to formulate general shell finite elements. One is a flat shell element which is constructed by superimposing the plate bending action and membrane action. A membrane behavior is not coupled with a plate bending behavior (bending and transverse shearing behaviors). The other is a continuum

mechanics based shell element (degenerated shell element) obtained by the degeneration of three-dimensional continuum mechanics [27]. Bending, membrane and transverse shearing behaviors are fully coupled. In this paper, the continuum mechanics based shell element is considered. Using these elements, the shell behavior can be represented more reliably for general shell structures. Also, a linear formulation can directly be extended to a general nonlinear analysis.

The geometry of a q-node continuum mechanics based triangular shell finite element is interpolated by [1,10]

$$\vec{x}(r,s,t) = \sum_{i=1}^q h_i(r,s) \vec{x}_i + \frac{t}{2} \sum_{i=1}^q a_i h_i(r,s) \vec{V}_n^i, \quad (2.10)$$

where $h_i(r,s)$ is the 2D shape function of the standard isoparametric procedure corresponding to node i , \vec{x}_i is the position vector for node i in the global Cartesian coordinate system, and a_i and \vec{V}_n^i denote the shell thickness and the director vector at node i , respectively.

The displacement interpolation of the element is obtained by

$$\vec{u}(r,s,t) = \sum_{i=1}^q h_i(r,s) \vec{u}_i + \frac{t}{2} \sum_{i=1}^q a_i h_i(r,s) (-\vec{V}_2^i \alpha_i + \vec{V}_1^i \beta_i), \quad (2.11)$$

in which \vec{u}_i is the nodal displacement vector in the global Cartesian coordinate system, \vec{V}_1^i and \vec{V}_2^i are unit vectors orthogonal to \vec{V}_n^i and to each other, and α_i and β_i are the rotations of the director vector \vec{V}_n^i about \vec{V}_1^i and \vec{V}_2^i at node i .

The linear terms of the displacement-based covariant strain components are given by

$$e_{ij} = \frac{1}{2} (\vec{g}_i \cdot \vec{u}_{,j} + \vec{g}_j \cdot \vec{u}_{,i}), \quad (2.12)$$

where

$$\vec{g}_i = \frac{\partial \vec{x}}{\partial r_i}, \quad \vec{u}_{,i} = \frac{\partial \vec{u}}{\partial r_i} \quad \text{with} \quad r_1 = r, \quad r_2 = s, \quad r_3 = t, \quad (2.13)$$

The displacement-based shell element shows the optimal convergence behavior in membrane-dominated shell problems. However, this shell element locks severely in bending-dominated shell problems.

2.3 Locking phenomenon and locking treatment

The solution of the shell finite elements converges slowly when the thickness becomes thin during bending-dominated and mixed shell behaviors. This phenomenon is called “locking”. The solution accuracy deteriorates in bending dominated and mixed shell behaviors because a finite element discretization cannot accurately approximate the pure bending displacement fields of shells. In the shell finite element analysis, membrane locking and shear locking occur. Membrane locking occurs when the geometry of a shell element has a curvature. If the geometry of a shell element is flat, no membrane locking occurs. Shear locking occurs regardless of a curvature of a shell element. In the following sections, several locking treatment schemes are presented [1, 2].

2.3.1 Reduced Integration

The reduced integration scheme reduces the order of Gaussian numerical integrations when constructing the stiffness matrix. The reduced integration scheme is divided into the uniformly reduced integration scheme and the selectively reduced integration scheme [28-30]. In the uniformly reduced integration scheme, a reduced order of Gaussian numerical integrations is applied to construct the stiffness matrix for all of the strain terms. Otherwise, in the selectively reduced integration scheme, a reduced order of the Gaussian numerical integrations is used to construct the stiffness matrix for the specific strain terms for which locking occurs. For example, in the 4-node shell element, only shear locking occurs. If reduced integration is used for the transverse shear strains of a 4-node shell element, the transverse shear strains are assumed to be constant as follows:

$$\tilde{e}_{rt} = e_{rt}(0,0,t), \quad \tilde{e}_{st} = e_{st}(0,0,t) \quad (2.14)$$

However, when using the reduced integration scheme, a spurious energy mode occurs. In some shell problems, the solutions can oscillate if a spurious energy mode dominates. Hence, the reduced integration scheme should be used with a stabilization technique [30].

2.3.2 Enhanced Assumed Strain method

The Enhanced Assumed Strain formulation is derived from the Hu-Washizu functional [31-34]. The internal energy part is given by

$$U_{EAS} = \int_V \frac{1}{2} (\mathbf{B}\vec{u} + \vec{\varepsilon}^E)^T \mathbf{C} (\mathbf{B}\vec{u} + \vec{\varepsilon}^E) dV \quad (2.15)$$

where \mathbf{B} is the strain-displacement matrix obtained by the original formulation, \vec{u} is the displacement vector, \mathbf{C} is the stress-strain law matrix, and $\vec{\varepsilon}^E$ is an enhanced strain vector with unknowns. The enhanced strain field is added to the inherent strain field obtained by the original formulation. The unknowns for the enhanced strain vector are condensed out on the element level.

2.3.3 Hellinger-Reissner principle

The Hellinger-Reissner functional (HR functional) is derived from the Hu-Washizu functional [1, 35, 36]. The internal energy part is given by

$$U_{HR} = \int_V \left(-\frac{1}{2} \vec{\varepsilon}^T \mathbf{C} \vec{\varepsilon} + \vec{\varepsilon}^T \mathbf{C} \partial_{\varepsilon} \vec{u} \right) dV \quad (2.16)$$

where $\vec{\varepsilon}$ is the strain vector, \mathbf{C} is the stress-strain law matrix, \vec{u} is the displacement vector, and ∂_{ε} is the differential operator on \vec{u} for strain calculations. It is important to note that the independent variables are the strains and displacements in this Hellinger-Reissner functional. An approximated strain field with unknowns is newly defined. The static condensation is performed for the unknowns on the element level.

2.3.4 Mixed Interpolation of Tensorial Components method

The MITC shell formulation is given by

$$\tilde{e}_{ij}(r, s, t) = \sum_{k=1}^{n_{ij}} h_{ij}^k(r, s) e_{ij} \Big|_{(r_{ij}^k, s_{ij}^k)} \quad (2.17)$$

where n_{ij} is the number of tying points to obtain the covariant strain components on the shell midsurface with coordinates (r_{ij}^k, s_{ij}^k) and h_{ij}^k is the assumed interpolation function corresponding to tying point k and satisfying

$$h_{ij}^k(r_{ij}^l, s_{ij}^l) = \delta_{kl}, \quad l = 1, \dots, n_{ij} \quad (2.18)$$

This tying procedure is performed on the element level. Note that to select the tying points and to construct the assumed strain interpolations are key to formulate the MITC shell elements successfully [1, 2].

The MITC method was first applied to develop the MITC4 quadrilateral shell finite element in the research of Dvorkin and Bathe [19]. Under the plate bending assumption, the MITC4 shell element becomes

the MITC4 plate bending element. Although the concept of the MITC4 plate bending element is similar to that of the plate elements developed by Hughes and Tezduyar and MacNeal, the MITC4 shell element is proposed for general shell analyses and assumed covariant strains are first used for the element[37, 38]. For the MITC4 element, the in-layer strain components are obtained from the displacement-based formulation and the transverse shear strains are assumed with the MITC method, as follows:

$$\tilde{e}_{rt} = \frac{1}{2}(1+s)e_{rt}^{(A)} + \frac{1}{2}(1-s)e_{rt}^{(C)}, \quad \tilde{e}_{st} = \frac{1}{2}(1+r)e_{st}^{(D)} + \frac{1}{2}(1-r)e_{st}^{(B)} \quad (2.19)$$

Tying positions (A)-(D) are presented in Fig. 2.2. Note that the stiffness matrix is obtained corresponding to the same nodal point degree of freedom as the displacement-based shell element without using the static condensation, like the elements based on the EAS method or the Hellinger-Reissner principle [31-36].

For the 9-node shell elements, Park and Stanley developed the 9-ANS shell element using the Assumed Nature Strain method which is close to the MITC method. In ANS method, assumed physical strain fields were obtained from the strains along selected co-ordinate lines [7]. Based on the MITC method, Bucalem and Bathe developed the 9-node MITC9 and 16-node MITC16 quadrilateral shell finite elements [21]. Afterward, Bathe et al. proposed an improved MITC9 shell element [22].

Lee and Bathe proposed a methodology with which to construct isotropic triangular shell elements based on the MITC method. The 3-node MITC3 shell element and 6-node MITC6 shell elements were developed by Lee and Bathe[10]. The improved MITC6 shell element was developed by Kim and Bathe [23].

The 3-node MITC3 triangular shell finite element shows much better predictive capability than the displacement-based 3-node triangular shell finite elements and other 3-node isotropic triangular shell finite elements [10, 11]. However, the degree of locking alleviation by MITC3 is not as great as that gained when using MITC4; that is, the accuracy of the solutions is not as good as that of the MITC4 quadrilateral shell finite elements due to locking.

2.4 The ideal shell finite element

In the finite element analysis, the variational formulation is determined as follows [1, 2]

Find $\vec{U}_h \in \vec{\Phi}_h$ such that

$$A_h(\vec{U}_h, \vec{V}_h) = \vec{F}(\vec{V}_h), \quad \forall \vec{V} \in \vec{\Phi}_h \quad (2.20)$$

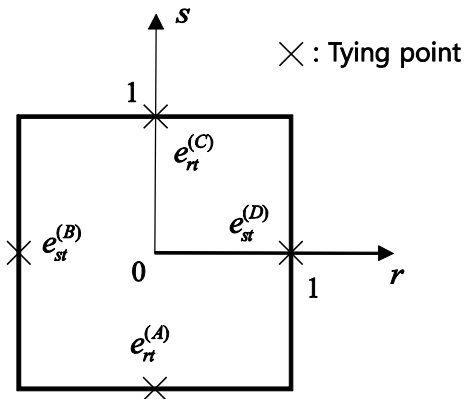


Fig. 2.2 Tying positions for the assumed transverse shear strain field of the MITC4 shell element.

where $A_h(\cdot, \cdot)$ denotes the bilinear forms for finite element discretization, $\vec{\Phi}_h$ is the space functions in which the finite element solution lies ($\vec{\Phi}_h \subset \vec{\Phi}$), \vec{U}_h is the finite element solution, and \vec{V}_h is the test function for finite element. $A_h(\vec{U}_h, \vec{V}_h)$ is given by

$$A_h(\vec{U}_h, \vec{V}_h) = \vec{V}_h^T (\int_V \mathbf{B}_h^T \mathbf{C}_h \mathbf{B}_h dV) \vec{U}_h. \quad (2.21)$$

where \mathbf{B}_h is the strain-displacement matrix [1, 2, 10, 26].

For general shell finite element analyses, the ideal shell finite elements satisfy the three aforementioned conditions. First, the ellipticity condition is defined as

$$\exists \alpha > 0 \text{ such that } \forall \vec{U}_h \in \vec{\Phi}_h, \quad A_h(\vec{U}_h, \vec{U}_h) \geq \alpha \|\vec{U}_h\|_1^2 \quad (2.22)$$

where α is a constant. This condition indicates that the given problems are solved using shell finite elements, that is, the shell finite element contains no spurious zero energy mode. Under unsupportable boundary conditions, the shell finite element contains exactly six zero eigenvalues corresponding to the rigid body modes.

Second, because finite element discretization is based on a mathematical model, the finite element solution should converge to the solution of the mathematical model as the element size h approaches zero. This condition is called consistency. The definition is as follows:

$$\lim_{h \rightarrow 0} \vec{U}_h = \vec{U} \quad \text{or} \quad \lim_{h \rightarrow 0} A_h(\vec{U}_h, \vec{U}_h) = A(\vec{U}, \vec{U}) \quad (2.23)$$

where $A_h(\cdot, \cdot)$ is the exact bilinear form of a mathematical model, and \vec{U} is the exact solutions [1, 2, 26].

Third, shell finite elements show uniformly optimal convergence behavior in bending-dominated problems or in mixed problems. This condition is called inf-sup condition. If shell finite elements satisfy inf-sup condition, the element is free from membrane locking and from shear locking, that is, the response is independent of the shell thickness. Although this condition is important, in general, it is not possible analytically to prove whether shell finite elements satisfy this condition. Hence, numerical tests are performed to verify whether shell elements satisfy this condition [1, 2, 26].

An additional condition is required for triangular shell finite elements. The response of the triangular shell elements should be the identical regardless of the node numbering sequence. This condition is called isotropy. The element stiffness matrices are independent of the node numbering sequence of a triangular shell element [10, 11].

When developing shell finite elements, it is extremely difficult to satisfy the above conditions. It is therefore necessary to soften the requirements as follows:

- No spurious zero energy mode (ellipticity condition)
- Satisfy the consistency condition
- No shear locking for plate bending problems
- Reliable convergence behavior for membrane-dominated shell problems
- Reliable convergence behavior for bending-dominated shell problems and mixed shell problems
- Easy to extend to a nonlinear formulation (simple formulation)
- Satisfy the isotropic condition for triangular shell elements

A practical range t/L is considered for bending-dominated shell problems and for mixed shell problems to soften the requirements [1, 2, 10].

Chapter 3. Improving the MITC3shell finite element

In this chapter, formulation of the 3-node displacement-based shell finite element is first reviewed. Then, the formulation of the MITC3 shell element is reviewed with the detail studies. In order to improve the performance of the MITC3 shell element, the Hellinger-Reissner functional is modified with a special approximated transverse shear strain field based on rotated contravariant bases[12].

3.1 Formulation of the 3-node displacement-based shell finite element

The geometry of a 3-node continuum mechanics based triangular shell finite element is interpolated by [10, 11]

$$\vec{x}(r,s,t) = \sum_{i=1}^3 h_i(r,s) \vec{x}_i + \frac{t}{2} \sum_{i=1}^3 a_i h_i(r,s) \vec{V}_n^i, \quad (3.1)$$

where $h_i(r,s)$ is the 2D shape function of the standard isoparametric procedure corresponding to node i , \vec{x}_i is the position vector for node i in the global Cartesian coordinate system, and a_i and \vec{V}_n^i denote the shell thickness and the director vector at node i , respectively; see Fig. 3.1.

The displacement interpolation of the element is obtained by

$$\vec{u}(r,s,t) = \sum_{i=1}^3 h_i(r,s) \vec{u}_i + \frac{t}{2} \sum_{i=1}^3 a_i h_i(r,s) (-\vec{V}_2^i \alpha_i + \vec{V}_1^i \beta_i), \quad (3.2)$$

in which \vec{u}_i is the nodal displacement vector in the global Cartesian coordinate system, \vec{V}_1^i and \vec{V}_2^i are unit vectors orthogonal to \vec{V}_n^i and to each other, and α_i and β_i are the rotations of the director vector \vec{V}_n^i about \vec{V}_1^i and \vec{V}_2^i at node i .

The linear terms of the displacement-based covariant strain components are given by

$$e_{ij} = \frac{1}{2} (\vec{g}_i \cdot \vec{u}_{,j} + \vec{g}_j \cdot \vec{u}_{,i}), \quad (3.3)$$

where

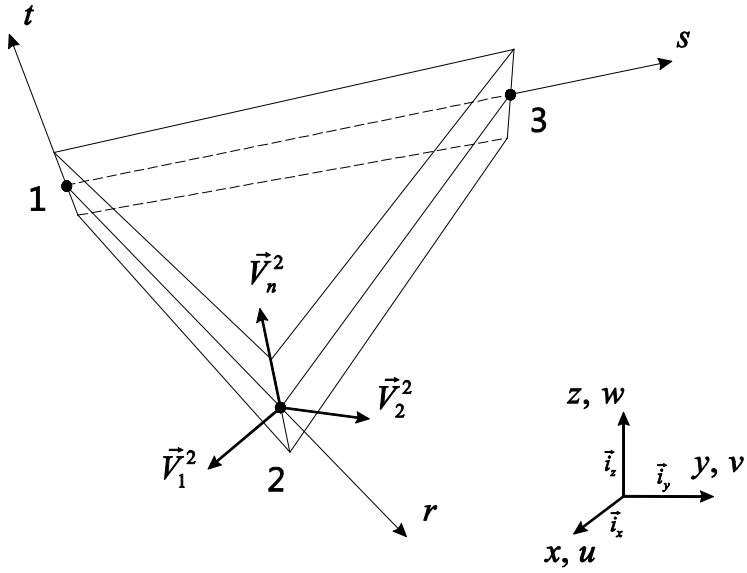


Fig. 3.1 A standard 3-node triangular continuum mechanics based shell finite element.

$$\vec{g}_i = \frac{\partial \vec{x}}{\partial r_i}, \quad \vec{u}_{,i} = \frac{\partial \vec{u}}{\partial r_i} \quad \text{with} \quad r_1 = r, \quad r_2 = s, \quad r_3 = t, \quad (3.4)$$

The covariant strain components can be expressed by

$$e_{ij} = \mathbf{b}_{ij} \vec{U}, \quad (3.5)$$

in which \mathbf{b}_{ij} is the covariant strain-displacement matrix and \vec{U} is the vector of nodal displacements and rotations, which include \vec{u}_k , α_k , and β_k .

The base vectors of the shell-aligned local Cartesian coordinate system are defined as follows

$$\vec{L}_{\bar{t}} = \frac{\vec{g}_t}{|\vec{g}_t|}, \quad \vec{L}_{\bar{r}} = \frac{\vec{g}_s \times \vec{L}_{\bar{t}}}{|\vec{g}_s \times \vec{L}_{\bar{t}}|}, \quad \vec{L}_{\bar{s}} = \vec{L}_{\bar{t}} \times \vec{L}_{\bar{r}}. \quad (3.6)$$

The strains (ε_{ij}) defined in the shell-aligned local Cartesian coordinate are calculated from the covariant strain components through the following relation,

$$\varepsilon_{ij}(\vec{L}_i \otimes \vec{L}_j) = e_{mn}(\vec{g}^m \otimes \vec{g}^n) \quad \text{with} \quad \vec{L}_1 = \vec{L}_{\bar{r}}, \quad \vec{L}_2 = \vec{L}_{\bar{s}}, \quad \vec{L}_3 = \vec{L}_{\bar{t}}, \quad (3.7)$$

In Eq. (3.7), the contravariant base vectors \vec{g}^j are given by

$$\vec{g}_i \cdot \vec{g}^j = \delta_i^j \quad \text{with} \quad \vec{g}^1 = \vec{g}^r, \quad \vec{g}^2 = \vec{g}^s, \quad \vec{g}^3 = \vec{g}^t, \quad (3.8)$$

where δ_i^j is the Kronecker delta in mixed form.

The strain vector defined in the shell-aligned local Cartesian coordinate system from the displacement-based shell formulation is

$$\vec{\varepsilon} = \mathbf{B}\vec{U}, \quad (3.9)$$

where $\vec{\varepsilon} = [\varepsilon_{rr} \quad \varepsilon_{ss} \quad 2\varepsilon_{rs} \quad 2\varepsilon_{st} \quad 2\varepsilon_{rt}]^T$.

3.2 Formulation of the MITC3 shell finite element

Since the 3-node triangular shell finite element is flat, the covariant in-plane strain components are calculated using Eqs. (3.1) to (3.3). However, the covariant transverse shear strain field is established using the MITC scheme. The additional transverse shear strain e_{qt} shown in Fig. 3.2 is considered to obtain the isotropic behavior [10]

$$\tilde{e}_{qt} = \frac{1}{\sqrt{2}}(\tilde{e}_{st} - \tilde{e}_{rt}). \quad (3.10)$$

The interpolation of the transverse shear strain field can be assumed as follows

$$\begin{aligned} \tilde{e}_{rt} &= a_1 + b_1 r + c_1 s, \\ \tilde{e}_{st} &= a_2 + b_2 r + c_2 s, \\ \tilde{e}_{qt} &= \frac{1}{\sqrt{2}}(\tilde{e}_{st} - \tilde{e}_{rt}) \quad (3.11) \\ &= \frac{1}{\sqrt{2}}\{(a_2 + b_2 r + c_2 s) - (a_1 + b_1 r + c_1 s)\}. \end{aligned}$$

Along the edges, the constant covariant transverse shear strain conditions shown in Fig. 3.3 are given by

$$\begin{aligned} \tilde{e}_{rt}(0,0) &= e_{rt}^{(1)}, \quad \tilde{e}_{rt}(1,0) = e_{rt}^{(1)}, \\ \tilde{e}_{st}(0,0) &= e_{st}^{(2)}, \quad \tilde{e}_{st}(0,1) = e_{st}^{(2)}, \\ \tilde{e}_{qt}(1,0) &= e_{qt}^{(3)} = \frac{1}{\sqrt{2}}(e_{st}^{(3)} - e_{rt}^{(3)}), \quad (3.12) \\ \tilde{e}_{qt}(0,1) &= e_{qt}^{(3)} = \frac{1}{\sqrt{2}}(e_{st}^{(3)} - e_{rt}^{(3)}). \end{aligned}$$

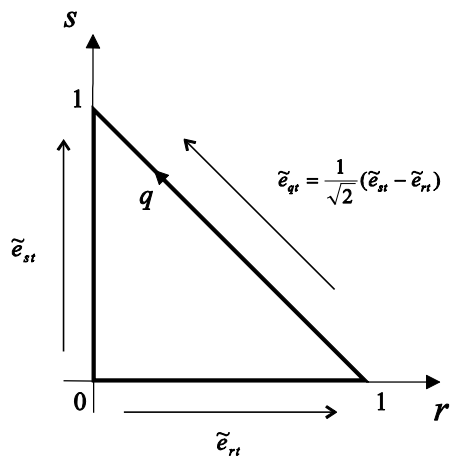


Fig. 3.2 Transverse shear strain relation

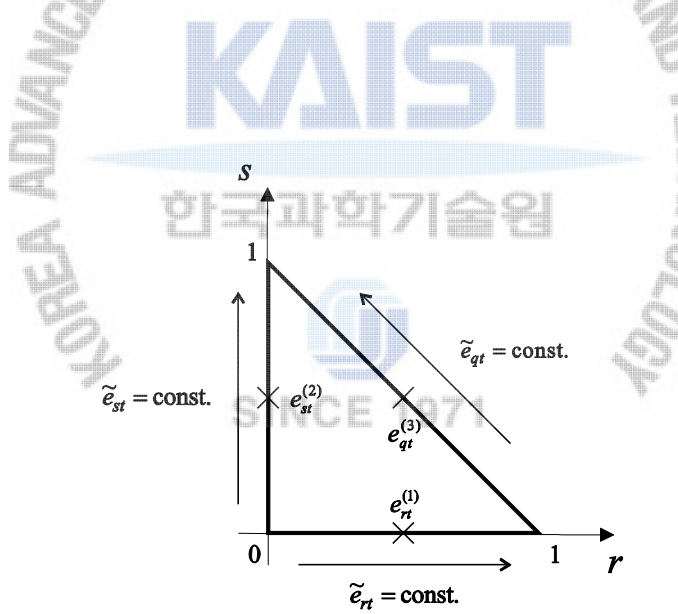


Fig. 3.3 Tying positions for the assumed transverse shear strain field of the MITC3 shell element. The constant transverse shear strain conditions are imposed along its edges.

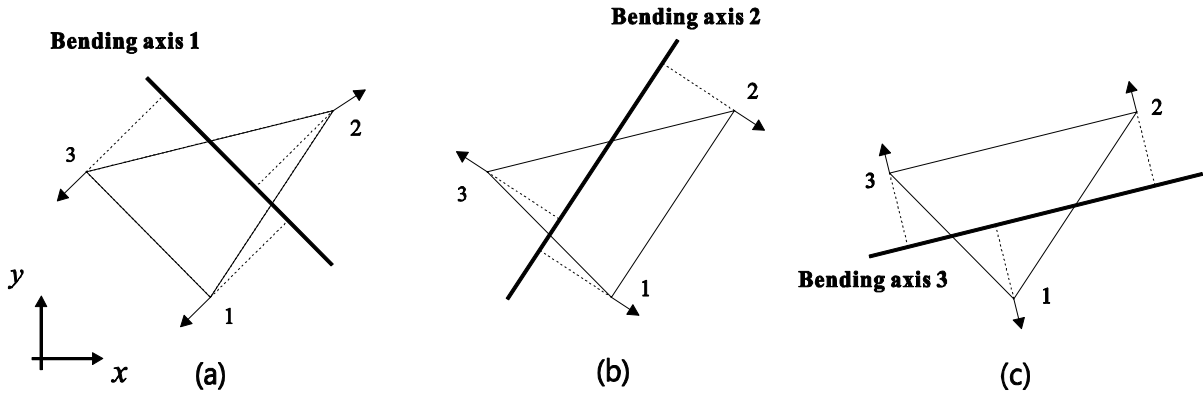


Fig. 3.4 The nodal displacement pattern of the physical strain energy modes at the top view. (a) Symmetrical bending mode 1. (b) Symmetrical bending mode 2. (c) Symmetrical bending mode 3.

The conditions in Eq. (3.12) is imposed to the interpolation in Eq. (3.11) to obtain the unknown coefficients. Finally, the assumed covariant transverse shear strain field is given by

$$\tilde{e}_{rt}^{MITC^3} = e_{rt}^{(1)} + cs, \quad \tilde{e}_{st}^{MITC^3} = e_{st}^{(2)} - cr, \quad (3.13)$$

where $c = (e_{rt}^{(3)} - e_{rt}^{(1)}) - (e_{st}^{(3)} - e_{st}^{(2)})$ and the tying points are shown in Fig. 3.3 [10].

The assumed covariant transverse shear strain field in Eq. (3.13) can be separated into the constant part and linear part. The three cases can be defined to represent the constant transverse shear strain field for the three bending modes. In the symmetrical bending mode 1 shown in Fig. 3.4(a), the covariant transverse shear strain field with the conditions and tying points shown in Fig. 3.5(a) is given by

$$\begin{aligned} \tilde{e}_{rt}^a &= e_{rt}^{(1)} \\ \tilde{e}_{st}^a &= e_{st}^{(3)} - e_{rt}^{(3)} + e_{rt}^{(1)} \end{aligned} \quad (3.14)$$

In the symmetrical bending mode 2 shown in Fig. 3.4(b), the covariant transverse shear strain field based on the conditions and tying points shown in Fig. 3.5(b) is obtained by

$$\begin{aligned} \tilde{e}_{rt}^b &= -e_{st}^{(3)} + e_{rt}^{(3)} + e_{st}^{(2)}, \\ \tilde{e}_{st}^b &= e_{st}^{(2)}. \end{aligned} \quad (3.15)$$

In the symmetrical bending mode 3 shown in Fig. 3.4(c), the covariant transverse shear strain field based on the conditions and tying points shown in Fig. 3.5(c) is given by

$$\tilde{e}_{rt}^c = e_{rt}^{(1)},$$

$$\tilde{e}_{st}^c = e_{st}^{(2)}. \quad (3.16)$$

The constant transverse shear strain field can be obtained by the average of the Eqs. (3.14)-(3.16)

$$\begin{aligned}\tilde{e}_{rt}^{const.} &= \frac{2}{3}(e_{rt}^{(1)} + \frac{1}{2}e_{st}^{(2)}) - \frac{1}{3}(e_{st}^{(3)} - e_{rt}^{(3)}), \\ \tilde{e}_{st}^{const.} &= \frac{2}{3}(e_{st}^{(2)} + \frac{1}{2}e_{rt}^{(1)}) + \frac{1}{3}(e_{st}^{(3)} - e_{rt}^{(3)}).\end{aligned}\quad (3.17)$$

For obtaining the assumed linear transverse shear strain field excluding the constant transverse shear strain filed, the assumed transverse shear strain field from the MITC3 shell formulation in Eq. (3.13) is subtracted by the constant transverse shear strain fields Eqs.(3.14)-(3.16) in the individual cases as follows

$$\tilde{e}_{rt}^{MITC3} - \tilde{e}_{rt}^a = cs, \quad \tilde{e}_{st}^{MITC3} - \tilde{e}_{st}^a = c(1-r), \quad (3.18)$$

$$\tilde{e}_{rt}^{MITC3} - \tilde{e}_{rt}^b = c(s-1), \quad \tilde{e}_{st}^{MITC3} - \tilde{e}_{st}^b = -cr, \quad (3.19)$$

$$\tilde{e}_{rt}^{MITC3} - \tilde{e}_{rt}^c = cs, \quad \tilde{e}_{st}^{MITC3} - \tilde{e}_{st}^c = -cr, \quad (3.20)$$

the Eqs. (3.18)-(3.20) are averaged to obtain the spatially isotropic transverse shear strain field

$$\begin{aligned}\tilde{e}_{rt}^{linear} &= \frac{1}{3}c(3s-1), \\ \tilde{e}_{st}^{linear} &= \frac{1}{3}c(1-3r).\end{aligned}\quad (3.21)$$

The assumed transverse shear strain field of the MITC3 element can be separated as follows

$$\begin{aligned}\tilde{e}_{rt}^{MITC3} &= \tilde{e}_{rt}^{const.} + \tilde{e}_{rt}^{linear} = \frac{2}{3}(e_{rt}^{(1)} + \frac{1}{2}e_{st}^{(2)}) - \frac{1}{3}(e_{st}^{(3)} - e_{rt}^{(3)}) + \frac{1}{3}c(3s-1), \\ \tilde{e}_{st}^{MITC3} &= \tilde{e}_{st}^{const.} + \tilde{e}_{st}^{linear} = \frac{2}{3}(e_{st}^{(2)} + \frac{1}{2}e_{rt}^{(1)}) + \frac{1}{3}(e_{st}^{(3)} - e_{rt}^{(3)}) + \frac{1}{3}c(1-3r).\end{aligned}\quad (3.22)$$

The constant part represents the constant transverse shearing mode. The linear part represents the in-plane twisting mode. The transverse strain fields Eqs.(3.14)-(3.16) and Eqs.(3.18)-(3.20) are automatically averaged with the Eq.(3.10) to satisfy the isotropic condition when constructing the assumed transverse shear strain field of the MITC3 element. Also, the MITC3 element can be developed with the mode decomposition, see Appendix A.

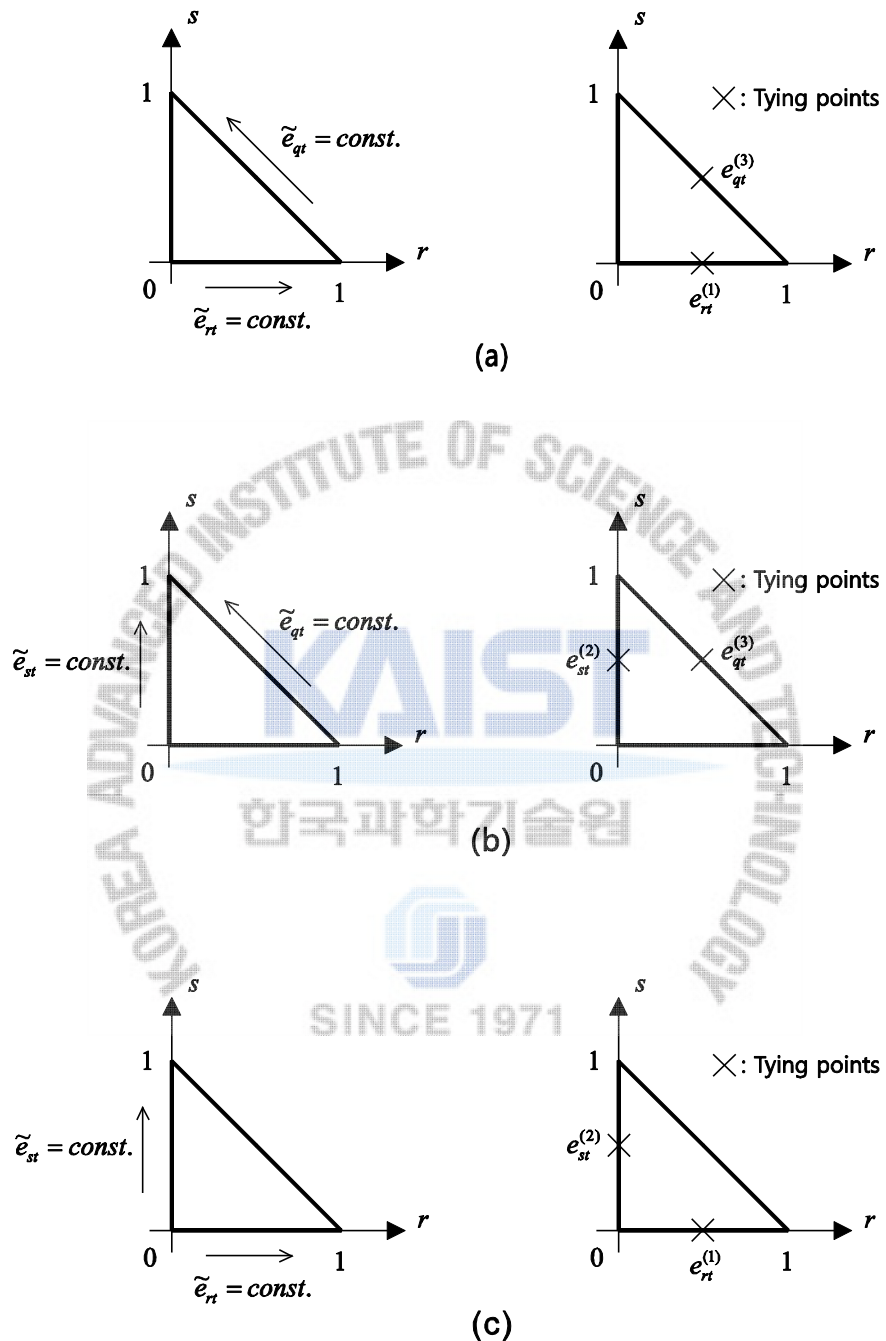


Fig. 3.5 The constant transverse shear strain condition and tying positions for the symmetrical bending modes,
 $\tilde{e}_{qt} = (\tilde{e}_{st} - \tilde{e}_{rt}) / \sqrt{2}$. (a) Symmetrical bending mode 1. (b) Symmetrical bending mode 2. (c) Symmetrical bending mode 3.

The assumed covariant transverse shear strain components of the MITC3 element can also be expressed by

$$\tilde{\epsilon}_{ij} = \tilde{b}_{ij} \vec{U}. \quad (3.23)$$

The covariant strains of the MITC3 shell finite element are transformed to the strains defined in the shell-aligned local Cartesian coordinate system $(\bar{L}_r, \bar{L}_s, \bar{L}_t)$

$$\tilde{\epsilon}^M = \mathbf{B}^M \vec{U} \quad \text{with} \quad \tilde{\epsilon}^M = [\epsilon_{rr}^M \quad \epsilon_{ss}^M \quad 2\epsilon_{rs}^M \quad 2\epsilon_{rt}^M \quad 2\epsilon_{st}^M]^T. \quad (3.24)$$

3.3 The Hellinger-Reissner principle for 3-node shell finite elements

The Hellinger-Reissner functional (HR functional), which is derived from the Hu-Washizu functional [1], is given by

$$\begin{aligned} \Pi_{HR} = & \int_V (-\frac{1}{2} \vec{\epsilon}^T \mathbf{C} \vec{\epsilon} + \vec{\epsilon}^T \mathbf{C} \partial_e \vec{u}) dV - \int_V \vec{u}^T \vec{f}^B dV - \int_{S_f} \vec{u}^{S_f T} \vec{f}^{S_f} dS \\ & - \int_{S_u} \vec{f}^{S_u T} (\vec{u}^{S_u} - \vec{u}_p) dS, \end{aligned} \quad (3.25)$$

where $\vec{\epsilon}$ is the strain vector, \mathbf{C} is the stress-strain law matrix, \vec{u} is the displacement vector, ∂_e is the differential operator on \vec{u} for strain calculations, \vec{f}^B is the vector for body forces, \vec{f}^{S_f} is the vector for applied surface tractions, \vec{u}_p is the vector for prescribed displacements, V is the volume of the body, S_f is the surface on which \vec{f}^{S_f} is applied, S_u is the surface on which \vec{u}_p is prescribed, \vec{u}^{S_f} is the displacement vector over S_f , \vec{u}^{S_u} is the displacement vector over S_u , and \vec{f}^{S_u} is the reaction vector calculated by the stresses on S_u . It is important to note that the independent variables are strains and displacements in this Hellinger-Reissner functional.

For the 3-node shell finite element formulation, the Hellinger-Reissner functional is changed to separate the bending and membrane strains and the transverse shear strains as follows

$$\begin{aligned} \Pi_{HR}^S = & \int_V (\frac{1}{2} \vec{\epsilon}_{bm}^T \mathbf{C}_{bm} \vec{\epsilon}_{bm} - \frac{1}{2} \vec{\gamma}^A T \mathbf{C}_\gamma \vec{\gamma}^A + \vec{\gamma}^A T \mathbf{C}_\gamma \vec{\gamma}) dV - \int_V \vec{u}^T \vec{f}^B dV - \int_{S_f} \vec{u}^{S_f T} \vec{f}^{S_f} dS \\ & - \int_{S_u} \vec{f}^{S_u T} (\vec{u}^{S_u} - \vec{u}_p) dS, \end{aligned} \quad (3.26)$$

where $\vec{\epsilon}_{bm}$ is the vector for the displacement-based bending and membrane strains, $\vec{\gamma}$ is the vector for the

displacement-based transverse shear strains, and $\vec{\gamma}^A$ is the vector for the approximated transverse shear strains with unknowns,

$$\vec{\varepsilon}_{bm} = \begin{pmatrix} \varepsilon_{rr} \\ \varepsilon_{ss} \\ 2\varepsilon_{rs} \end{pmatrix}, \quad \vec{\gamma} = \begin{pmatrix} 2\varepsilon_{st} \\ 2\varepsilon_{rt} \end{pmatrix}, \quad \vec{\gamma}^A = \begin{pmatrix} 2\varepsilon_{st}^A \\ 2\varepsilon_{rt}^A \end{pmatrix}, \quad (3.27)$$

and all the strain components are defined in the shell-aligned local Cartesian coordinate system to satisfy the material stress-strain law for shells.

In Eq. (3.26), C_{bm} is the stress-strain law matrix for the bending and membrane strains and C_γ is the stress-strain law matrix for the transverse shear strains,

$$C_{bm} = \frac{E}{1-\nu^2} \begin{bmatrix} 1 & \nu & 0 \\ \nu & 1 & 0 \\ 0 & 0 & \frac{1-\nu}{2} \end{bmatrix}, \quad C_\gamma = \frac{E}{1-\nu^2} \begin{bmatrix} k\frac{1-\nu}{2} & 0 \\ 0 & k\frac{1-\nu}{2} \end{bmatrix}, \quad (3.28)$$

where E , ν , and k are Young's modulus, Poisson's ratio, and a shear correction factor, respectively. In this work, we use $k = 1.0$.

In general, $\vec{\varepsilon}_{bm}$ and $\vec{\gamma}$ come from the 3-node displacement-based shell formulation; that is, $\vec{\varepsilon}_{bm}$ and $\vec{\gamma}$ are obtained by Eq. (3.9)

$$\vec{\varepsilon}_{bm} = \begin{pmatrix} \varepsilon_{rr} \\ \varepsilon_{ss} \\ 2\varepsilon_{rs} \end{pmatrix} = \mathbf{B}_{bm}\vec{U}, \quad \vec{\gamma} = \begin{pmatrix} 2\varepsilon_{st} \\ 2\varepsilon_{rt} \end{pmatrix} = \mathbf{B}_\gamma\vec{U}. \quad (3.29)$$

The approximated transverse shear strain field ($\vec{\gamma}^A$) is constructed with the appropriate interpolation with unknowns ($\vec{\alpha}$),

$$\vec{\gamma}^A = \begin{pmatrix} 2\varepsilon_{st}^A \\ 2\varepsilon_{rt}^A \end{pmatrix} = \mathbf{B}_\gamma^A\vec{\alpha}, \quad (3.30)$$

Finally, the unknown variables in Eq. (3.26) are the nodal displacements and rotations (\vec{U}) and the approximated transverse shear strains ($\vec{\alpha}$). The effectiveness of the shell finite element formulation based on the Hellinger-Reissner principle highly depends on how the interpolation function is constructed in Eq. (3.30).

3.4 Formulation of the MITC3-HR shell finite element

We here modify the Hellinger-Reissner functional in Eq. (3.26) as follows

$$\begin{aligned}\Pi_{HR}^M = & \int_V \left(\frac{1}{2} \vec{\varepsilon}_{bm}^M{}^T \mathbf{C}_{bm} \vec{\varepsilon}_{bm}^M - \frac{1}{2} \vec{\gamma}^A{}^T \mathbf{C}_\gamma \vec{\gamma}^A + \vec{\gamma}^A{}^T \mathbf{C}_\gamma \vec{\gamma}^M \right) dV - \int_V \vec{u}^T \vec{f}^B dV - \int_{S_f} \vec{u}^{S_f T} \vec{f}^{S_f} dS \\ & - \int_{S_u} \vec{f}^{S_u T} (\vec{u}^{S_u} - \vec{u}_p) dS,\end{aligned}\quad (3.31)$$

with

$$\vec{\varepsilon}_{bm}^M = \begin{pmatrix} \varepsilon_{rr}^M \\ \varepsilon_{ss}^M \\ 2\varepsilon_{rs}^M \end{pmatrix} = \mathbf{B}_{bm}^M \vec{U}, \quad \vec{\gamma}^M = \begin{pmatrix} 2\varepsilon_{st}^M \\ 2\varepsilon_{rt}^M \end{pmatrix} = \mathbf{B}_\gamma^M \vec{U}, \quad \vec{\gamma}^A = \begin{pmatrix} 2\varepsilon_{st}^A \\ 2\varepsilon_{rt}^A \end{pmatrix} = \mathbf{B}_\gamma^A \vec{\alpha}, \quad (3.32)$$

in which $\vec{\varepsilon}_{bm}^M$ and $\vec{\gamma}^M$ are the vector for the bending and membrane strains and the vector for the transverse shear strains obtained by Eq. (3.24) in the MITC3 shell finite element formulation.

This is a very important modification of the Hellinger-Reissner functional. As a result, the new element, MITC3-HR, is based on the formulation of the MITC3 shell finite element. It provides strong potential to improve the MITC3 shell finite element. Since the MITC formulation can be represented by the Hellinger-Reissner principle [39], the Hellinger-Reissner principle is, in effect, used twice in our formulation.

Another important part for successful development is the approach taken to construct the approximated transverse strain field, which should retain the isotropic property as well as improve the predictive capability of the MITC3 shell finite element. For the construction of $\vec{\gamma}^A$ in Eq. (3.32), we use a special approximated transverse shear strain field introduced on the rotated contravariant base vectors. The components of $\vec{\gamma}^A$ are given by

$$\begin{aligned}2\varepsilon_{rt}^A &= 2\tilde{e}_{st}^A[(\vec{g}^s \cdot \vec{L}_r)(\vec{g}^t \cdot \vec{L}_r) + (\vec{g}^t \cdot \vec{L}_r)(\vec{g}^s \cdot \vec{L}_r)] + 2\tilde{e}_{rt}^A[(\vec{g}^r \cdot \vec{L}_r)(\vec{g}^t \cdot \vec{L}_r) + (\vec{g}^t \cdot \vec{L}_r)(\vec{g}^r \cdot \vec{L}_r)], \\ 2\varepsilon_{st}^A &= 2\tilde{e}_{st}^A[(\vec{g}^s \cdot \vec{L}_s)(\vec{g}^t \cdot \vec{L}_s) + (\vec{g}^t \cdot \vec{L}_s)(\vec{g}^s \cdot \vec{L}_s)] + 2\tilde{e}_{rt}^A[(\vec{g}^r \cdot \vec{L}_s)(\vec{g}^t \cdot \vec{L}_s) + (\vec{g}^t \cdot \vec{L}_s)(\vec{g}^r \cdot \vec{L}_s)]\end{aligned}\quad (3.33)$$

with

$$\tilde{e}_{rt}^A = \alpha_2 + \alpha_3 s, \quad \tilde{e}_{st}^A = \alpha_1 - \alpha_3 r, \quad (3.34)$$

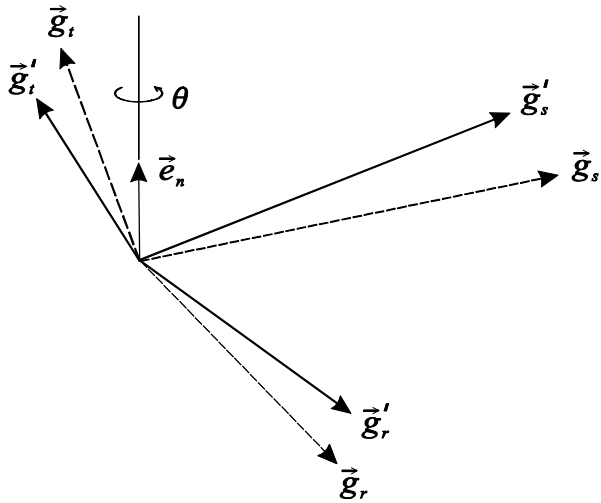


Fig. 3.6 The rotated covariant base vectors for the MITC3-HR shell finite element. The dotted and solid vectors correspond to the original and rotated covariant base vectors, respectively.

in which $\vec{g}^{r'}$, $\vec{g}^{s'}$ and $\vec{g}^{t'}$ are the rotated contravariant base vectors and α_1 , α_2 , and α_3 are the unknown variables for the approximated covariant transverse shear strains. Here, it is important to note that the type of interpolation functions in Eq. (3.13) is the same as that of the interpolation functions used in Eq. (3.34), which belong to a "rotated Raviart-Thomas space".

In order to calculate the rotated contravariant base vectors, as shown in Fig. 3.5, we first rotate the three covariant base vectors about the vector (\vec{e}_n) normal to the midsurface ($t = 0$) of the shell element

$$\vec{g}'_i = \cos\theta \vec{g}_i + (1 - \cos\theta)(\vec{g}_i \cdot \vec{e}_n)\vec{e}_n + (\vec{e}_n \times \vec{g}_i)\sin\theta \quad (3.35)$$

with

$$\vec{e}_n = \frac{\vec{g}_r \times \vec{g}_s}{|\vec{g}_r \times \vec{g}_s|}, \quad (3.36)$$

in which \vec{g}_i are the covariant base vectors ($i = r, s$ and t) evaluated by Eq. (3.4) at the integration points of the shell element, and θ is the angle of rotation about \vec{e}_n . The rotated contravariant base vectors are then calculated by

$$\vec{g}'_i \cdot \vec{g}^{j'} = \delta_i^j. \quad (3.37)$$

Note that \vec{e}_n is a constant vector, because the midsurface of the 3-node shell element is flat.

Invoking $\delta \Pi_{HR}^M = 0$ in Eq. (3.31), we obtain corresponding to $\delta \vec{u}$

$$\int_V (\delta \vec{\varepsilon}_{bm}^M{}^T \mathbf{C}_{bm} \vec{\varepsilon}_{bm}^M + \delta \vec{\gamma}^M{}^T \mathbf{C}_\gamma \vec{\gamma}^A) dV = \int_V \delta \vec{u}^T \vec{f}^B dV, \quad (3.38)$$

and corresponding to $\delta \vec{\gamma}^A$

$$\int_V \delta \vec{\gamma}^A{}^T \mathbf{C}_\gamma (\vec{\gamma}^M - \vec{\gamma}^A) dV = 0. \quad (3.39)$$

Eqs.(3.38) and (3.39) are changed to thematrix form with Eq.(3.32)

$$\begin{bmatrix} \mathbf{K}_{uu} & \mathbf{K}_{ue} \\ \mathbf{K}_{eu} & \mathbf{K}_{ee} \end{bmatrix} \begin{pmatrix} \vec{U} \\ \vec{\alpha} \end{pmatrix} = \begin{pmatrix} \vec{R} \\ \vec{0} \end{pmatrix} \quad (3.40)$$

and, using the static condensation on $\vec{\alpha}$, the stiffness matrix of the MITC3-HR shell finite element is finally given as

$$\mathbf{K} = \mathbf{K}_{uu} - \mathbf{K}_{ue} \mathbf{K}_{ee}^{-1} \mathbf{K}_{ue}^T \quad (3.41)$$

with

$$\begin{aligned} \mathbf{K}_{uu} &= \int_V \mathbf{B}_{bm}^M{}^T \mathbf{C}_{bm} \mathbf{B}_{bm}^M dV, \\ \mathbf{K}_{ue} &= \int_V \mathbf{B}_\gamma^M{}^T \mathbf{C}_\gamma \mathbf{B}_\gamma^A dV, \\ \mathbf{K}_{ee} &= - \int_V \mathbf{B}_\gamma^A{}^T \mathbf{C}_\gamma \mathbf{B}_\gamma^A dV. \end{aligned} \quad (3.42)$$

After obtaining the nodal displacement solution \vec{U} , $\vec{\alpha}$ is given by

$$\vec{\alpha} = -\mathbf{K}_{ee}^{-1} \mathbf{K}_{ue}^T \vec{U}, \quad (3.43)$$

and the strains are then calculated by $\vec{\varepsilon}_{bm}^M$ and $\vec{\gamma}^A$ in Eq. (3.32), and the stresses are obtained using the stress-strain law in Eq. (3.28).

3.5 Basic numerical tests

In this section, the results of three basic tests of the MITC3-HR shell finite elements are presented. Table 3.1 presents the results of the basic tests.

Table 3.1 Results of basic numerical tests

Element	Zero energy mode test	Isotropy test	Patch test
MITC3-HR	Pass	Pass	Pass

3.5.1 Strain energy mode tests

We count how many zero eigenvalues exist in the stiffness matrix of a single unsupported element. The single shell finite element should pose exactly six zero eigenvalues, corresponding to the six physical rigid body modes. When a shell finite element has additional zero eigenvalues corresponding to spurious energy modes, the stability of the solutions cannot be guaranteed [1].

The MITC3-HR shell finite element passes the zero energy mode test except for the case where the angle θ in Eq. (3.35) is 90 deg and the element has a uniform thickness. Tables 3.1 and 3.2 present the eigenvalues of the strain energy modes of the MITC3-HR shell finite element according to the rotation angle (θ) of the contravariant base vector for the plate bending problem shown in Fig. 3.7(a) when t/L is 0.001 and 0.0001 (uniform thickness). We use $L = 1.0$, $E = 1.7472 \times 10^7$ and $\nu = 0.3$. Because the eigenvalues change with the order of $(t/L)^3$ in the modes 7, 8 and 9, these modes are easily identified as bending modes. After investigating the strain distributions by the modes 11 and 13, it is found that these two modes include both transverse shear and bending modes.

When the angle $\theta = 0$, all of the eigenvalues of the MITC3-HR shell finite element are identical to those of the MITC3 shell finite element. As the angle θ increases to 90 deg, the 10th eigenvalue decreases. Fig. 3.8 presents the 10th mode shapes ($\theta = 89$ deg) of the displacement based 3-node, MITC3 and MITC3-HR shell finite elements. It is very interesting to note that, while the 10th strain energy mode of the displacement based 3-node shell element is the pure in-plane twisting mode (Fig. 3.8(a)), the 10th modes of MITC3 and MITC3-HR shell finite elements includes a bending mode as well as the pure in-plane twisting mode (Fig. 3.8(b) and (c)). Also, we note that the 10th mode shape of the MITC3-HR shell finite elements varies depending on the angle θ , but the change is very small, see Fig. 3.8(b) and (c).